Solar-Powered Wireless Temperature Sensor Based on UWB RFID with Self-Calibration

Angel Ramos, *Student Member, IEEE*, David Girbau, *Senior Member, IEEE*, Antonio Lazaro, *Member, IEEE*, Ana Collado, *Senior Member, IEEE*, and Apostolos Georgiadis, *Senior Member, IEEE*

Abstract—This paper presents a solar-powered wireless temperature sensor based on time-coded ultra-wideband radiofrequency identification. A negative temperature coefficient resistor acts as the sensing element. It controls the current of a PIN diode connected to an ultra-wideband scattering antenna. The wireless sensor is self-calibrated using a narrowband tone, making its performance independent of the distance or orientation between the reader and the sensor. A consumption of 82 µA is demonstrated. An error under 0.6 °C within a 35 °C − 70 °C temperature range is obtained for most of the cases.

Index Terms—Ultra-wideband, PIN diode, NTC, solar cell, energy harvesting

I. INTRODUCTION

RADIOFREQUENCY identification (RFID) is used to remotely identify targets, and it is widely used in logistics, medicine, industry and other fields [1]. RFID consists of a reader that interrogates one or more tags. The reader remotely acquires the tag's identification (ID) by means of a radiofrequency (RF) link. Currently, chip-based RFID tags at UHF band are the most used for identification.

The American Federal Communications Commission (FCC) allocated an Ultra-Wideband (UWB) spectrum from 3.1 to 10.6 GHz in 2002 [2]. Since then, a great interest has grown in developing technologies that use UWB, due to the advantages associated to its large bandwidth [3]. UWB has good immunity to multipath propagation, it is barely affected by narrowband interferences, and it has a high range resolution and penetration in materials. Furthermore, the bandwidth allocation and masks of UWB are very similar worldwide, with small differences depending on the region [2][4]. Therefore, low-cost UWB circuitry is expected in the next years.

RFID systems were initially designed only to collect identification information from the tag. A lot of research has been done to improve RFID capabilities: the aim is to obtain not only the ID, but also physical parameters of the tag's environment. These parameters are sensed by the tag itself, which becomes a wireless sensor. One way to achieve it is by embedding a sensor into a chipless tag [5-6]. Another way is by using chip-based tags. To this purpose, a standard Gen2 UHF tag has been integrated with a sensor in [7]. Other solutions use custom chip-based systems [8].

Several wireless temperature sensors have been recently presented. In [9] a temperature sensor is integrated into a battery-free standard UHF RFID tag. In [10] another temperature sensor is integrated in a tag which uses a 2.3 GHz signal to send data and a 450 MHz signal to receive power. In [11] a temperature and photo sensor is integrated in a custom UHF system. In [12-13] passive, microcontoller-based UHF EPC Gen2 compliant sensing platforms are proposed. Read ranges of 5 m in [12], and 10 m (fully passive) or 22 m (battery-assisted) in [13] are reported.

In [7-13] cases, narrow band signals have been used. However, recent works [14-18] have demonstrated that ultra-wideband signals can also be used for RFID applications.

This work presents a semi-passive RFID sensor based on a time-coded UWB backscatterer (UWB antenna connected to a delay line) [18-19]. Here, a PIN diode loads the delay line. The PIN diode current is controlled by a negative temperature resistor (NTC). Then, the backscattered response of the tag is modulated in amplitude by the temperature. However, since the signal received at the reader not only contains this information of temperature, but is affected by the tag-reader distance, orientation or environment (clutter), a calibration mechanism is also included. It is based on a parallel 2.43 GHz link which switches the sensor between the measurement, calibration and clutter removal states. In addition, big efforts are being done during last years to power wireless sensors and RFID tags by means of green energies, such as solar energy [20-21]. In this direction, a solar cell is integrated to power up the sensor.

This paper is organized as follows. Section II presents the working principle and theory of the UWB sensor and the modulation of its response as a function of the temperature. Section III describes the reader and the implemented tag. Section IV presents the calibration procedure and the measured results. Section V discusses the power consumption

and complexity of the tag in front of other approaches. Finally, Section VI draws the conclusions.

II. OPERATION THEORY

A. Time-coded UWB backscattering

Fig. 1. shows a scheme of the UWB backscatterer and the signals sent from the reader (TX) and backscattered at the tag (RX). The tag is composed by a UWB antenna connected to a delay line which is, in turn, loaded with a low-cost PIN diode (model NXP BAP64-03).

The reader transmits a UWB pulse $p(t)$. When it hits the tag, a portion of it is reradiated back and another portion propagates inside the tag. Then, the tag response is composed by the sum of these two terms: the structural mode (s_{Str}) and the tag mode (s_{Tag}). The structural mode depends on the tag shape, size and material. The tag mode depends on the radiation pattern of the antenna and the load connected to it. The antenna can be modelled as a two-port network [15] terminated with the PIN diode-loaded transmission line. The response can be expressed as (1):

$$s(t) = s_{Str.}(t) + s_{Tag}(t) = \alpha S_{11}(t) * p(t) * \delta(t - \tau_P)$$
$$+ \alpha \Gamma_{LOAD} g(t) * p(t) * \delta(t - \tau_P - \tau_L) \quad (1)$$

where α is the round-trip attenuation factor due to the propagation in free space, τ_P is the round-trip time delay between tag and reader, $\tau_P = 2L/v$ is the round-trip propagation delay along the transmission line (with length L and propagation velocity v), $g(t)$ is the inverse Fourier transform of $S_{12}S_{21}$, δ is the Dirac delta function and $*$ denotes the convolution operator. The approximation is valid considering that Γ_{LOAD} is real. The term $S_{11}*p(t)$ is the response associated to the structural mode and $\Gamma_{LOAD} g(t) * p(t)$ is the response associated to the tag mode. Moreover, $\Gamma_{LOAD} = (Z_{LOAD} - Z_C)/(Z_{LOAD} + Z_C)$ is the reflection coefficient due to the load Z_{LOAD} at the end of the transmission line, being $Z_C = 50 \ \Omega$ the characteristic impedance of the transmission line.
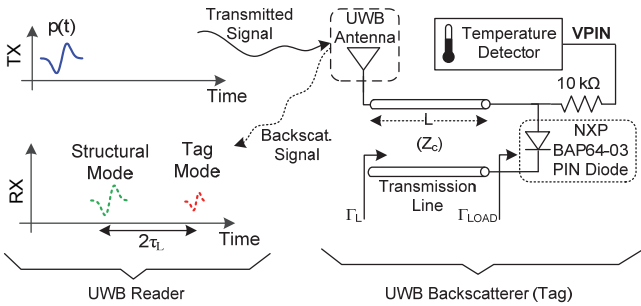

Fig. 1. Scheme of the sent and received signals between the reader and tag.

B. Modulating the tag mode with a PIN diode

For the purpose of adding sensing capability to the tag, this work aims to modulate the amplitude of the tag mode. This can be done by modulating the load Z_{LOAD}, since the resistance of the PIN diode in forward polarization depends on the current that flows through it [22]. This current is controlled by a temperature detector circuit.

Fig. 2a shows the measured backscattered signal of a time-coded chipless tag loaded with the BAP64-03 PIN diode, biased with a 10 kΩ resistor, as shown in Fig. 1. This measurement is performed with the Time Domain PulsON P400 MRM radar, connected to two UWB antennas, with a distance tag-reader of 30 cm. The diode bias voltage (V_{PIN}) is manually swept from 0 to 3.3 V (current between 0 and 260 µA). Each line represents a different current. In Fig. 2b. the continuous Wavelet transform (CWT) has been applied to the measured signal to improve the signal-to-noise ratio [16]. All signals are normalized with respect to their own maximum amplitude, which is the structural mode. It can be observed that the tag modes amplitudes vary depending on the current that flows through the diode.
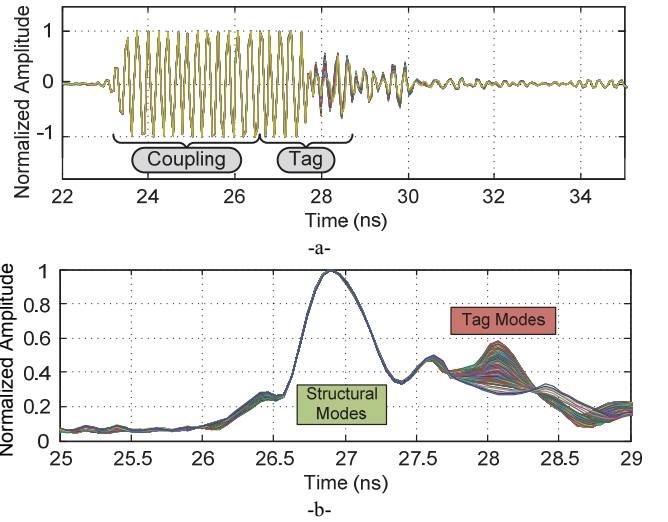

Fig. 2. Measured time-domain response of the tag depending on the diode current. (a) Raw signal, (b) signal after applying the CWT.

Fig. 3 shows the structural to tag mode ratio as a function of the diode current. The ratio goes from a large value at 0 µA, which equals to an open circuit state ($Z_{LOAD} \to \infty$), to a low value at around 55 µA, which equals to a matched load state ($Z_{LOAD} \approx Z_C$). It is important to note that the ratio is not equal to zero at the minimum of the curve, mainly because of parasitic effects of the diode. The shaded area in Fig. 3 shows a low-power consumption zone of the curve that can be exploited. Considering a 10 kΩ polarization resistor, this zone corresponds to a bias voltage range between 0.45 V and 1.15 V, and current between 0 µA and 55 µA.
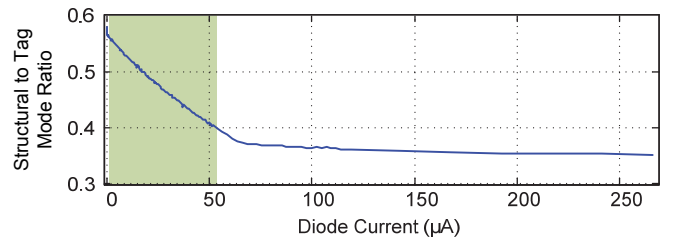
Fig. 3. Structural to tag mode ratio as a function of the diode forward current.

III. System and Sensor Design

Fig. 4 shows a basic scheme of the system. It consists of a reader and the sensor. The reader uses a narrowband 2.43 GHz signal to change the tag state in order to perform the calibration and clutter removal for each temperature measurement. The reader also uses the UWB radar (Time Domain PulsON P400) to collect the tag answer by backscattering. The 2.43 GHz link has two objectives. First, clutter is obtained and removed for each temperature measurement, and then it does not matter if it is not stationary. Second, a calibration curve can be obtained for each measurement and temperature can be derived for any distance/angle between reader and tag, a serious limitation in chipless RFID tags [6].
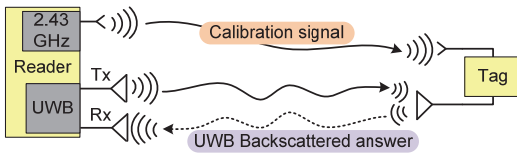

Fig. 4. Scheme of the proposed system.

The system works as shown in the flow diagram of Fig. 5. First, the reader measures the background scene with the UWB radar, which consists on the tag being deactivated. Next, the reader sends a 2.43 GHz calibration signal with a "Calibration" state. The tag sets itself to a known calibration state, which is independent of the temperature. Then, the reader collects the backscattered calibration answer via UWB. After, the reader sends another calibration signal with a "Temperature" state. The tag sets itself to a state which, in this case, depends on the temperature, and the reader collects the backscattered answer via UWB.
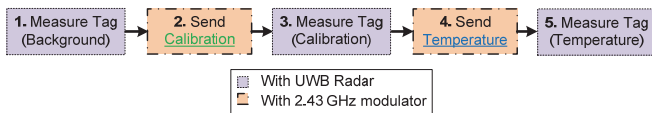

Fig. 5. Flow diagram of one temperature measurement.

A. Sensor design

Fig. 6 shows a scheme of the sensor. It consists of four main blocks. The UWB backscatterer block (see Section II.A) communicates the sensor with the reader. It is based on a broadband eccentric annular monopole antenna connected to a delay line. The delay line length L is chosen to separate the structural and tag modes with a round-trip delay of about 1 ns. The ground plane has significant effects on planar UWB monopole antenna properties. A negative impact on antenna performance is also obtained when it is connected to long meander-shaped delay lines. To solve these problems two slots have been introduced between the antenna and the ground plane similarly as done in [6]. They are marked with yellow ellipses in Fig. 7b. A detector circuit block, which depends on the 2.43 GHz signal received from the reader, activates the calibrator circuit block. The calibrator circuit block delivers the three states. These states permit three consecutive

measurements with the UWB backscatterer, which are used for clutter removal, calibration and temperature measurement. The temperature is sensed by means of the NTC. Finally, there is a power supply circuit block which consists of a solar cell and a regulator, that generates the bias voltages and voltage thresholds for the state comparators. Photographs of the fabricated sensor tag are shown in Fig. 7. It is manufactured on Rogers RO4003C substrate. The tag size is 15.7 cm x 8.2 cm.
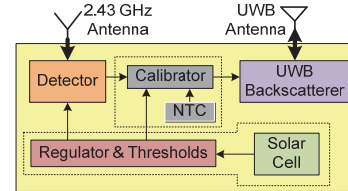

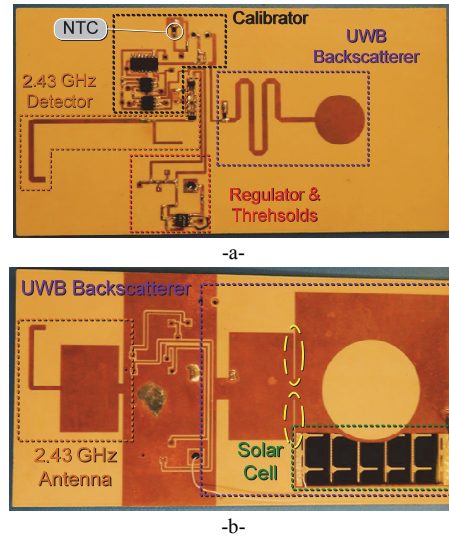Fig. 6. Scheme of the designed tag.

Fig. 7. Fabricated tag, (a) top face and (b) bottom face.

B. Reader

A scheme of the designed reader is shown in Fig. 8. It consists of the 2.43 GHz modulator which sets the tag at different states, and the UWB radar that sends the pulsed signal to the tag and collects the backscattered signal with the measurement. The modulator is based on a 2.43 GHz oscillator, followed by a power amplifier and a monopole antenna. The transmitted power is +20 dBm at the ISM band, which falls within the European regulation. In order to generate two different calibration signals from the modulator, a PIC 16F1827 microcontroller is used as a buffer to activate or deactivate the oscillator. In this manner, an On-Off-Keying (OOK) signal is generated. The two calibration signals consist of a "Calibration" state, with a duty cycle of the 30% of the OOK, and a "Temperature" state, with a duty cycle of 70% of the OOK. The control PC communicates with the microcontroller through a USB-RS232 interface.
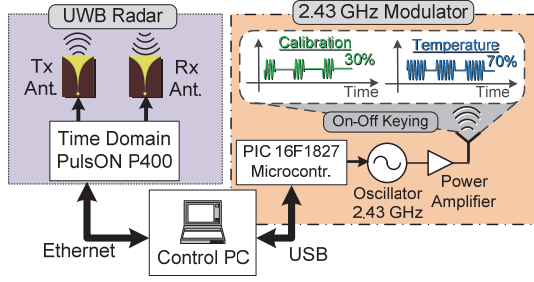
Fig. 8. Scheme of the reader.

C. 2.43 GHz Detector

The detector is shown in Fig. 9. It consists of a 2.43 GHz dipole antenna connected to an Avago HSMS-2852 Schottky diode rectifier through a matching network. A 100 pF DC block capacitor is placed between the 2.43 GHz antenna and the matching network. The matching network consists of a shunt-connected, open-ended L-shaped stub and a series connected transmission line. At the output of the Schottky diode, a 1 nF capacitor and an 820 kΩ resistor are shunt-connected to obtain the rectified voltage from the diode. A Texas Instruments TLV2401 low-power operational amplifier is used as a comparator, providing a 0 V output when the rectifier does not detect voltage and 3 V when it does. The comparator threshold is obtained by an RC estimator (R = 82 kΩ, C = 1 μF). Using this configuration, the detector is robust to external interferers (such as Wi-Fi or Bluetooth), and can theoretically be used up to a 12.6 m distance [17]. Finally, the output of the comparator is connected to another RC estimator (R = 820 kΩ, C = 1 μF), which provides the mean value of the OOK signal between 0 V and 3 V. This mean value depends on the duty cycle, but not on the tag-to-reader distance.
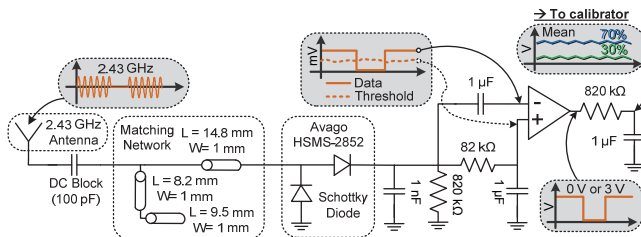

Fig. 9. Scheme of the 2.43 GHz detector circuit.

D. Calibrator

The calibrator circuit is shown in Fig. 10a. A time diagram of the main signals involved in the calibrator circuit is shown in Fig. 10b. The circuit consists on a (first) Texas Instruments TLV2402 dual channel operational amplifier. Each channel acts as a comparator (C1 and C2), detecting whether the mean value of the OOK signal exceeds two predefined voltage thresholds V_{th1} and V_{th2}. If the mean value exceeds V_{th1} but is below V_{th2} (meaning a 30% duty cycle), a second TLV2402 and a Maxim MAX4523 switch are powered from the first TLV2402 output 30P. This corresponds to the "Calibration" state. In this case, amplifier B of the second TLV2402 provides a V_{cal} = 1.33 V voltage for the switch input COM2. B

is operating as a buffer to independize the V_{th2} threshold from V_{cal}. Finally, since the mean value is not above V_{th2}, the switch will provide V_{cal} at its output (V_{PIN}).

When the mean value exceeds V_{th2} (meaning a 70% duty cycle), the first TLV2402 outputs (30P and 70P) are at up state and the switch output (V_{PIN}) will correspond to input COM1. This corresponds to the "Temperature" state. The COM1 voltage depends on the value of the AVX NB20R00684 NTC SMD Thermistor. This COM1 temperature-dependent voltage is generated from the non-inverting amplifier structure of the second TLV2402 amplifier A. It has a gain of 2.2 set by the 220 kΩ and 100 kΩ resistors. The non-inverting input IN1+ is the voltage at the NTC in parallel with a 150 kΩ resistor, minus the voltage drop at the 820 kΩ series resistor. With these values, the output voltage 1OUT is between 0.6 V at 70 ºC (NTC = 420 kΩ) and 1.2 V at 35 ºC (NTC = 98 kΩ). It corresponds to the shaded zone of the of Fig. 4. The output of the MAX4523 switch is ended with a 1 MΩ resistor and a 35 pF capacitor due to manufacturer's requirements.
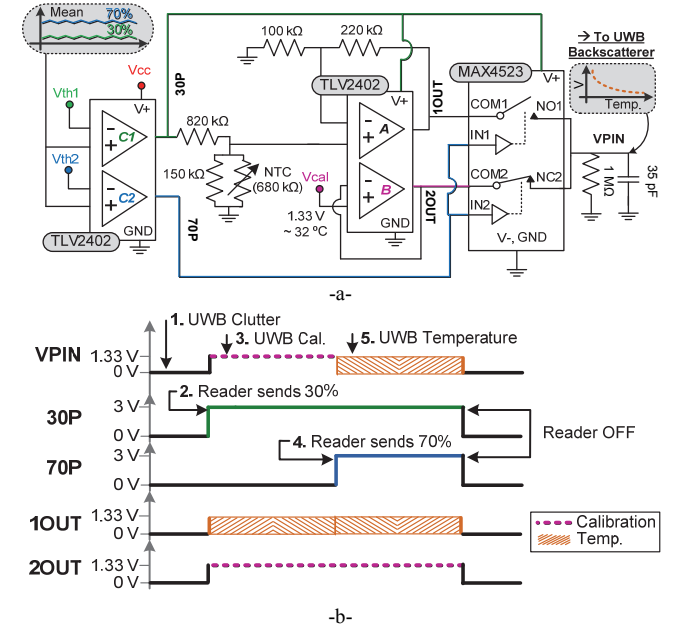

Fig. 10. (a) Scheme of the calibrator circuit. (b) Time diagram of the signals.

E. Solar cell integration

The flexible amorphous silicon Power Film SP3-37 solar cell was selected for this work. The specifications of SP3-37 are an open circuit voltage V_{oc} = 4.1 V and a short circuit current I_{sc} = 28 mA, when illuminated by a light source complying with the standard AM1.5G global solar irradiance spectrum [23], T = 25 º and 1 sun (= 100 mW/cm^2) irradiance.

The SP3-37, shown in Fig. 11, is rectangular with dimensions 64 mm by 37 mm. In Fig. 11 one can see the positive and negative terminals of the solar cell as well as a number of conductive strips on its top surface. The cell itself is a small solar module consisting of five smaller cells isolated by each of the four intermediate horizontal conductive strips which are electrically connected in series. Each of the individual cells provides an open circuit voltage V_{oc} = 0.82 V

and short circuit current I_{sc} = 28 mA, set by the width of the cell.

The integration of solar cells with antennas has been originally proposed in [24]. The placement of a solar cell on top of a printed antenna does not affect the antenna performance provided that the area of the conductive surface of the antenna where the current density is high, such as near the feed point and the radiating edges, is not covered by the cell [24]. This fact allows to significantly reduce the total area required for the circuitry and solar cells, allowing for more a compact system implementation.

The solar cell used to power the sensor was therefore integrated on the UWB antenna ground plane. In order to avoid placing the solar cell near the antenna feed point and due to the presence of the circular disc aperture in the ground plane limiting the available area, it was necessary to cut the original cell along its length into two pieces capable to produce an open circuit voltage V_{oc} = 4.1 V and a short circuit current I_{sc} = 14 mA under 1 sun irradiance. As one can see in the inset of Fig. 11, it was necessary to further shape the two pieces in order to conform to the ground plane conductive area leading to a non-uniform width which results in a slightly reduced current capability. The current capability of each solar cell piece alone is sufficient to power the sensor circuitry.
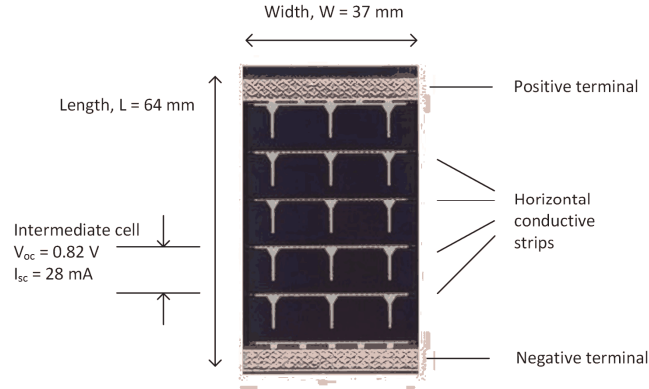

Fig. 11. Power Film SP3-37 solar cell.

Fig. 12 shows the measured $|S_{11}|$ parameter of the UWB monopole with and without two solar cells. There are two measurements, one with the solar cells placed with a 1 mm gap between the circular slot and the cell and the other with a 2 mm gap. The antenna performance is not affected at all by the cells.
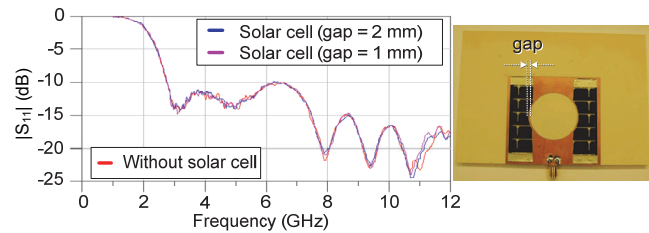

Fig. 12. Measured $|S_{11}|$ parameter of the tag antenna without and with the solar cell.

Each cell has sufficient current capability to power the sensor tag. As a result only one cell was placed in the final

circuit prototype as it can be observed in Fig. 7. It should be noted that the negative terminal of the cell is directly soldered on the ground plane conductor while the positive terminal of the cell is connected to the circuit supply using an insulated wire.

F. Regulator and thresholds

The output of the solar cell is connected to a Linear Technologies LT1763 (LT1763CS8#PBF) variable voltage regulator. As shown in Fig. 13, It is adjusted to provide a 3 V output with two resistors of 500 kΩ and 750 kΩ , according to the manufacturer: $Vcc = 1.22(1 + R_2 / R_1) + I_{ADJ}R_2$, where I_{ADJ} = 30 nA typically. The thresholds needed for the detector and calibrator circuits are obtained using a simple resistive circuit.
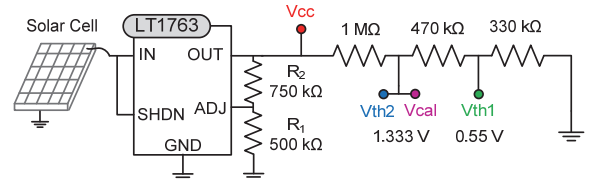

Fig. 13. Scheme of the solar cell connected to the regulator and the resistive values for the thresholds.

IV. RESULTS

A. Calibration and temperature measurement

To evaluate the validity of the system, the tag performance is measured. Fig. 14a shows the unprocessed (RAW) signals of the tag response at a 40 cm distance, heating the tag up to 70 ºC with a heatgun and letting it cool down on still air to 35 ºC . Fig. 14a also shows the RAW signals for the background state (s_{back}), and the calibration state (where the PIN diode is biased with V_{cal}). A very large coupling contribution from the reader's TX to RX antenna is present before the tag response, since the separation between the reader's antennas is smaller than the reader-sensor distance. Also, some clutter is present due to reflections with surrounding objects. Fig. 14b shows the zoomed area corresponding to the tag response. The structural modes, as shown, remain identical for all the possible temperatures of the tag. On the contrary, the tag modes amplitudes change. The tag mode with the largest amplitude corresponds to the s_{back} state, which corresponds to the tag measurement without any current flowing through the diode, that is without any 2.43 GHz calibration signal sent to the tag. With this background measurement, the clutter and coupling contributions can be diminished without having to measure the empty-room response. To enhance the tag modes, for each measurement s_i (which contains the coupling contribution, the structural and tag modes, and clutter) the background s_{back} is subtracted as shown in Fig. 15. It can be clearly observed that the coupling contribution and clutter have been diminished in front of the tag mode. Since the structural mode is also the same for the background (the tag is not removed from the scene), it is also removed.
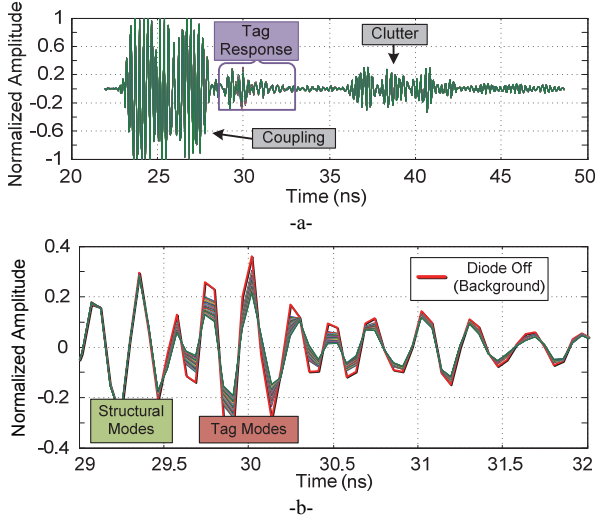
Fig. 14. (a) Unprocessed time domain signals for the tag response from 35 ºC to 70 ºC. (b) Zoomed tag response.
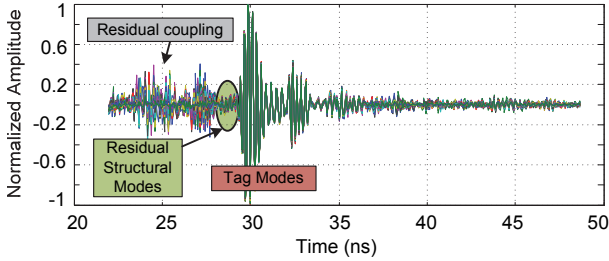

Fig. 15. Tag response after subtracting the background signal.

Fig. 16 shows the background-subtracted signal from Fig. 15 after applying the CWT. As shown in the inset of Fig. 16, the amplitude grows when temperature changes from 35 ºC to 70 ºC. All amplitudes are normalized with respect to the calibration state.
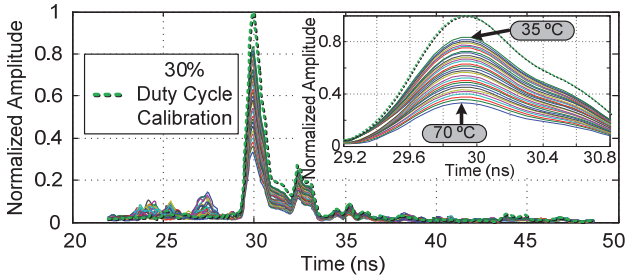

Fig. 16. Tag response after subtracting the background signal and applying the CWT.

The calibration to temperature ratio can be defined as the ratio between the amplitude in the calibration state and the amplitude in the temperature measurement state. It can be obtained by detecting the peaks of the tag modes in Fig. 16. Fig. 17 shows the calibration to temperature ratio as a function of the diode current, which varies from 15 µA to 60 µA.
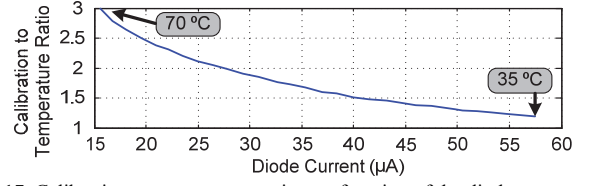

Fig. 17. Calibration to temperature ratio as a function of the diode current.

The real temperature is obtained with a reference wired multimeter (Agilent 34410A) from the output voltage of the calibrator. Since the elements in the circuit are known, the equivalent NTC resistance R_{NTC} for a given voltage can be calculated. In this manner, the wireless performance is compared to the same NTC sensor when it is measured with a stable, wired instrument. The real temperature T for a given resistance can be obtained using the manufacturer's values (R_n = 680 kΩ at 25 ºC, β = 4400, T_2 = 298 K):

$$T = \left[\frac{\ln\left(R_{NTC}/R_n \right)}{\beta} + \frac{1}{T_2} \right]^{-1} \quad [K] \qquad (2)$$

Fig. 18 shows the calibration to temperature ratio for 8 random measurements at distances tag-reader from 40 cm to 150 cm, as a function of the real temperature. The mean ratio for these 8 measurements is also shown. As it can be observed, all the measurements are very similar.

Fig. 19 shows the real temperature as a function of the mean ratio from Fig. 18, and a 5th degree polynomial regression. The polynomial regression coefficients are used to obtain the estimated temperature from the ratios. This step is required only once in order to obtain the temperature calibration curve of the sensor.

Finally, Fig. 20 shows the estimated (measured) temperature as a function of the real temperature for the 8 measurements. The estimated temperature is calculated for each of the 8 measurements using their ratios and the polynomial regression parameters from Fig. 19. An ideal curve is also shown, where the estimated temperature equals the real temperature. As shown, most of the measurements are very close to the real temperature, validating the functionality of the system, independently of the distance and angle.
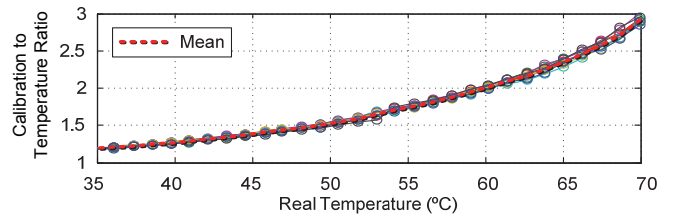

Fig. 18. Calibration to temperature ratio as a function of the real temperature for 8 random measurements from 40 cm to 150 cm.
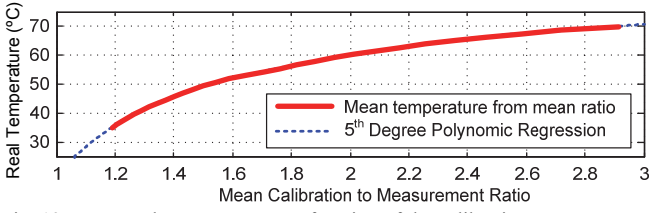
Fig. 19. Mean real temperature as a function of the calibration to temperature ratio and corresponding 5th degree polynomic regression.
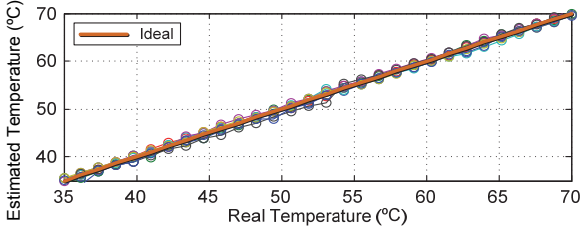

Fig. 20. Estimated temperature as a function of the real temperature for 8 random measurements from 40 cm to 150 cm.

B. Error study

For the purpose of characterizing the error obtained with the tag sensor, a study is carried out next. Fig. 21a shows an histogram obtained from 500 measurements at a fixed temperature (29 ℃) and distance (40 cm). In this case, 88% of the measurements are under 0.6 ℃ of error. Fig. 21b shows another histogram for the 8 random measurements of Section IV.A. Tag-reader distances are between 40 cm and 150 cm and the temperature range is from 35 ℃ to 70 ℃. Here, 84% of the measurements are within a 0.6 ℃ of error. Finally, Fig. 22 shows the mean relative error of Fig. 20b. In comparison with other works where a UWB radar is used as the reader [6], these results are similar for the fixed temperature/distance cases. The main advantage of the sensor proposed in this work is that the error for a fixed case is very similar to the error for the case of the sensor being moved. In chipless sensors [6] the error is greatly increased when the distance or orientation between the tag and the reader changes, and they require a calibration curve for each tag-reader distance/orientation, something impractical in real applications, and something which is not required in this sensor.
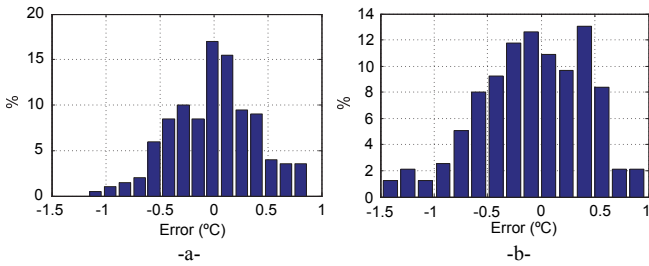

Fig. 21. (a) Absolute temperature error as a function of the real temperature for 8 random measurements from 40 cm to 150 cm.
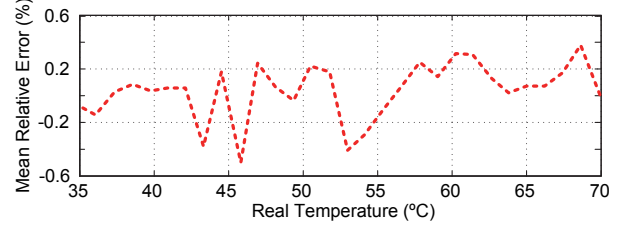

Fig. 22. Mean relative temperature error as a function of the real temperature for 8 random measurements from 40 cm to 150 cm.

V. POWER CONSUMPTION AND DISCUSSION

The presented tag needs to work by its own power source (in this case, solar energy). Since the consumption is a major concern in autonomous sensors, a study is carried out here. Table 1 shows the current consumption of each element in the tag circuitry. As expected, the most consuming element is the PIN diode, which draws up to 75 µA when it is in a calibration state. There are three possible combinations, depending on whether the tag is on a "Standby" state, waiting to receive the calibration signal by the reader, a "Temperature" state, or a "Calibration" state. Their corresponding currents, I_{Stdby}, I_{Temp} and I_{Cal}, respectively, are calculated next (3)(4)(5). As shown, the maximum current consumption is around 82 µA.

$$I_{Stdby} = I_{Th} + 3I_{Cmp} = 4.3042 \text{ µA} \tag{3}$$

$$I_{Temp} = \begin{cases} I_{Th} + 5I_{Cmp} + I_{Sw} + I_{Dmm} = 22.06 \text{ µA (at 70 ℃)} \\ I_{Th} + 5I_{Cmp} + I_{Sw} + I_{DmM} = 62.06 \text{ µA (at 35 ℃)} \end{cases} \tag{4}$$

$$I_{Cal} = I_{Th} + 5I_{Cmp} + I_{Sw} + I_{Dc} = 82.06 \text{ µA} \tag{5}$$

TABLE I
CURRENT CONSUMPTION BY ELEMENT

Element	Symbol	Current (µA)	
		Minimum	Maximum
Threshold resistive divisor	I_{Th}		1.66
TLV240X	I_{Cmp}		0.88/channel
MAX4523	I_{Sw}		1
PIN Diode (Temperature)	I_{Dmm}, I_{DmM}	15 (at 70 ℃)	55 (at 35 ℃)
PIN Diode (Calibration)	I_{Dc}		75

It is important to note that the current consumption of this setup is noticeably lower than the one required by setups based on a microcontroller, such as [17]. Even though that the tag in [17] consumes 75 µA while answering, it requires 250 µA to operate the Analog-to-Digital converter module (ADC). This module is required to acquire the output voltage from the conditioning circuit of the NTC. Therefore, the total consumption of the microcontroller-based approach is about 325 µA when using the ADC, which is higher than the 82 µA in this work. Other commercial microcontrollers such as the Texas Instruments MSP430 have lower ADC consumption (75 µA). However considering the total consumption, it would sum up to around 150 µA, which is still above the 82 µA presented in this work.

The complexity of this system is also lower than the microcontroller approach, which makes it a good candidate to integrate all the discrete elements into a single chip.

VI. CONCLUSION

This work has presented a semi-passive solar-powered temperature sensor based on a time-coded UWB tag. This is a low-cost and battery-less solution based on simple off-the-shelf components. A calibration mechanism has been integrated allowing for clutter removal and making the measurement of temperature completely independent of the reader-tag distance and angle. A sensor power consumption of 82 μA is demonstrated with an error under 0.6 ºC within a temperature range 35-70 ºC. It is measured using a UWB radar as reader at distances up to 150 cm.

References

[1] K. Finkenzeller, "RFID Handbook: Fundamentals and Applications in Contactless Smart Cards, Radio Frequency Identification and Near-Field Communication," Wiley 3rd Ed., 2010.

[2] Federal Communications Commission, "Revision of Part 15 of the Commission's Rules Regarding Ultra-Wideband Transmission Systems," http://hraunfoss.fcc.gov/edocs_public/attachmatch/FCC-02-48A1.pdf, Feb. 14, 2002 [Mar. 27, 2012].

[3] R. J. Fontana, "Recent System Applications of Short-Pulse Ultra-Wideband (UWB) Technology," IEEE Trans. on Microwave Theory and Tech., Vol. 52, No. 9, pp. 2087-2104, Sep. 2004.

[4] European Telecommunications Standard Institute, "Ultra Wide Band," http://www.etsi.org/website/technologies/UltraWideBand.aspx, 2011, [Mar. 27, 2012].

[5] S. Shrestha, M. Balachandran, M. Agarwal, V. V. Phoha, and K. Varahramyan, "A Chipless RFID Sensor System for Cyber Centric Monitoring Applications," IEEE Trans. on Microwave Theory and Techniques, Vol. 57, No. 5, pp. 1303-1309, May 2009.

[6] D. Girbau, A. Ramos, A. Lazaro, S. Rima, and R. Villarino, "Passive Wireless Temperature Sensor Based on Time-Coded UWB Chipless RFID Tags," IEEE Transactions on Microwave Theory and Techniques, Vol. 60, No. 11, pp. 3623-3632, 2012.

[7] J. Yin, J. Yi, M. K. Law, et al. "A System-on-Chip EPC Gen-2 Passive UHF RFID Tag With Embedded Temperature Sensor," IEEE Journal of Solid-State Circuits, Vol. 45, No. 11, pp. 2404-2420, Nov. 2010.

[8] R. Vykas, V. Lakafosis, A. Rida, N. Chaisilwattana, S. Travis, J. Pan, and M. M. Tentzeris, "Paper-Based RFID-Enabled Wireless Platforms for Sensing Applications," IEEE Trans. on Microwave Theory and Tech., Vol. 57, No. 5, pp. 1370-1382, 2009.

[9] A. P. Sample, D. J. Yeager, P. S. Powledge, A. V. Mamishev, and J. R. Smith, "Design of an RFID-Based Battery-Free Programmable Sensing Platform," IEEE Transactions on Instrumentation and Measurement, Vol. 57, No. 11, pp. 2608-2615, 2008.

[10] F. Kocer, and M. P. Flynn, "An RF-powered, wireless CMOS temperature sensor," IEEE Sensors Journal, Vol. 6, No. 3, pp. 557-564, 2006.

[11] N. Cho, S-J. Song, S. Kim, S. Kim, H-J. Yoo, "A 5.1-μW UHF RFID tag chip integrated with sensors for wireless environmental monitoring," Proc. 31st European Solid-State Circuits Conference 2005, pp. 279-282, 2005.

[12] D. De Donno, L. Catarinucci, and L. Tarricone, "Enabling Self-Powered Autonomous Wireless Sensors with New-Generation I2C-RFID Chips," 2013 IEEE MTT-S International Microwave Symposium Digest (MTT), Seattle, WA, June 2013.

[13] D. De Donno, L. Catarinucci, and L. Tarricone, "RAMSES: RFID Augmented Module for Smart Environmental Sensing," IEEE Transactions on Instrumentation and Measurement, Vol. 63, No. 7, pp. 1701-1708, July 2014.

[14] P. K. Gentner, M. Wiessflecker, G. Hofer, and C. F. Mecklenbrauker, "Bandwidth Reconfigurable UWB RFID Tag with On-Chip Antenna," 2011 Loughborough Antennas & Propagation Conference, pp. 1-3, Nov. 2011.

[15] A. Ramos, A. Lazaro, D. Girbau, and R. Villarino, "Time-Domain Measurement of Time-Coded UWB Chipless RFID Tags," Progress in Electromagnetics Research, Vol. 116, pp. 313-331, 2011.

[16] A. Lazaro, A. Ramos, D. Girbau, and R. Villarino, "Chipless UWB Tag Detection Using Continuous Wavelet Transform," IEEE Ant. and Wireless Prop. Letters, Vol. 10, pp. 520-523, 2011.

[17] A. Ramos, A. Lazaro, and D. Girbau, "Semi-Passive Time-Domain UWB RFID System," IEEE Transactions on Microwave Theory and Techniques, Vol. 61, No. 4, pp. 1700-1708, 2013.

[18] D. Dardari and R. D'Errico, "Passive Ultrawide Bandwidth RFID", IEEE Global Telecommunications Conference (GLOBECOM), pp. 1–6, 2008.

[19] S. Hu, Y. Zhou, C. L. Law, and W. Dou, "Study of a Uniplanar Monopole Antenna for Passive Chipless UWB-RFID Localization System," IEEE Trans. on Antennas and Prop., Vol. 58, No. 2, pp. 271-278, Feb. 2010.

[20] S. Kim, A. Georgiadis, A. Collado, and M. M. Tentzeris, "An Inkjet-Printed Solar-Powered Wireless Beacon on Paper for Identification and Wireless Power Transmission Applications," IEEE Transactions on Microwave Theory and Techniques, Vol. 60, No. 12, Part. 2, pp. 4178-4186, 2012.

[21] A. Georgiadis, A. Collado, S. Kim, L. Hoseon, and M. M. Tentzeris, "UHF solar powered active oscillator antenna on low cost flexible substrate for wireless identification applications," 2012 IEEE MTT-S International Microwave Symposium Digest, pp. 1-3, 2012.

[22] NXP Semiconductors, "BAP64-03 Silicon PIN Diode," Product specification, Feb. 2004.

[23] American Society for Testing and Materials (ASTM) Terrestrial Reference Spectra for Photovoltaic Performance Evaluation, http://rredc.nrel.gov/solar/spectra/am1.5/

[24] M. Tanaka, R. Suzuki, Y. Suzuki, K. Araki, "Microstrip antenna with solar cells for microsatellites," in Proc. 1994 IEEE International Symposium on Antennas and Propagation (AP-S), pp.786-789 vol.2, 20-24 June 1994

Angel Ramos (S'14) received the BS in Telecommunication Engineering and the MS in Electronic Engineering from Universitat Rovira i Virgili (URV), Tarragona, Spain, in 2010 and 2011, respectively. He is pursuing his PhD with the Department of Electronics, Electrics and Automatics Engineering, URV.

David Girbau (M'04-SM'13) received the BS in Telecommunication Engineering, MS in Electronics Engineering and PhD in Telecommunication from Universitat Politècnica de Catalunya (UPC), Barcelona, Spain, in 1998, 2002 and 2006, respectively. From February 2001 to September 2007 he was a Research Assistant with the UPC. From September 2005 to September 2007 he was a Part-Time Assistant Professor with the Universitat Autònoma de Barcelona (UAB). Since October 2007 he is a Full-Time Professor at Universitat Rovira i Virgili (URV). His research interests include microwave devices and systems, with emphasis on UWB, RFIDs and RF-MEMS.

Antonio Lázaro (M'07) was born in Lleida, Spain, in 1971. He received the M.S. and Ph.D. degrees in telecommunication engineering from the Universitat Politècnica de Catalunya (UPC), Barcelona, Spain, in 1994 and 1998, respectively. He then joined the faculty of UPC, where he currently teaches a course on microwave circuits and antennas. In July 2004 he joined the Department of Electronic Engineering, Universitat Rovira i Virgili, Tarragona, Spain. His research interests are microwave device modeling, on-wafer noise measurements, monolithic microwave integrated circuits (MMICs), low phase noise oscillators, MEMS, and microwave systems.

Ana Collado (M'07–SM'12) received the M.Sc. and Ph.D. degrees in Telecommunications Engineering from the University of Cantabria, Spain, in 2002 and 2007 respectively. She is currently a Senior Research Associate and the Project Management Coordinator at the Technological Telecommunications Center of Catalonia (CTTC), Barcelona, Spain where she performs her professional activities. Her professional interests include active antennas, substrate integrated waveguide structures, nonlinear circuit design, and energy harvesting and wireless power transmission (WPT) solutions for self-sustainable and energy efficient systems.

She has participated in several national and international research projects and has co-authored over 70 papers in journals and conferences. Among her activities she has collaborated in the organization of several international workshops in different countries of the European Union and also a Training School for PhD students. She is a Marie Curie Fellow of the FP7 project Symbiotic Wireless Autonomous Powered system (SWAP). She was finalist in the 2007 IEEE International Microwave Symposium student paper competition. She serves in the Editorial Board of the Radioengineering Journal and she is currently an Associate Editor of the IEEE Microwave Magazine and a member of the IEEE MTT-26 Technical Committee.

Apostolos Georgiadis (S'94–M'03-SM'08) was born in Thessaloniki, Greece. He received the B.S. degree in physics and M.S. degree in telecommunications from the Aristotle University of Thessaloniki, Greece, in 1993 and 1996, respectively. He received the Ph.D. degree in electrical engineering from the University of Massachusetts at Amherst, in 2002.

He is currently a Senior Research Associate and Coordinator of the Microwave Systems and Nanotechnology Department at Centre Tecnològic de Telecomunicacions de Catalunya (CTTC), Barcelona, Spain, where he is involved in active antennas and antenna arrays and more recently with RFID technology and energy harvesting.

Dr. Georgiadis serves as a reviewer for several journals including IEEE Transactions on Antennas and Propagation, and IEEE Transactions on Microwave Theory and Techniques. He was the Chairman of EU COST Action IC0803, RF/Microwave communication subsystems for emerging wireless technologies (RFCSET). He was the Chair of the 2011 IEEE RFID-TA Conference and co-Chair of the 2011 IEEE MTT-S IMWS on Millimeter Wave Integration Technologies. He is the Chair of the IEEE MTT-S TC-24 RFID Technologies and Member of IEEE MTT-S TC-26 Wireless Energy Transfer and Conversion. He serves at the Editorial board of the Radioengineering Journal and as an Associate Editor of the IEEE Microwave and Wireless Components Letters and IET Microwaves Antennas and Propagation Journals.